

NO-A184 784

NAVIER-STOKES CALCULATIONS OF HOVERING ROTOR FLOWFIELDS 1/1

(U) JAI ASSOCIATES INC MOUNTAIN VIEW CA

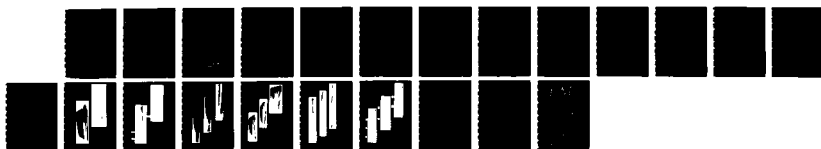
G R SRINIVASAN ET AL 19 AUG 87 ARO-21731 4-EG-S

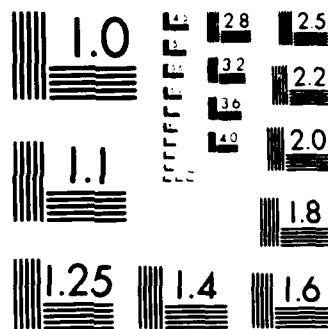
UNCLASSIFIED

DAAG29-85-C-0002

F/G 20/4

NL





MICROCOPY RESOLUTION TEST CHART
NATIONAL BUREAU OF STANDARDS-1963-A

SECURITY CLASSIFICATION OF THIS PAGE

DOCUMENTATION PAGE

AD-A184 784

REPORT SECURITY CLASSIFICATION

Unclassified

2a. SECURITY CLASSIFICATION

2b. DECLASSIFICATION/DOWNGRADING SCHEDULE

4. PERFORMING ORGANIZATION REPORT NUMBER(S)

6a. NAME OF PERFORMING ORGANIZATION

JAI Associates

6b. OFFICE SYMBOL
(If applicable)

1b. RESTRICTIVE MARKINGS

3. DISTRIBUTION/AVAILABILITY OF REPORT

Approved for public release;
distribution unlimited.

5. MONITORING ORGANIZATION REPORT NUMBER(S)

ARO 21731.4-EG-S

6c. ADDRESS (City, State, and ZIP Code)

Mountain View, CA 94043-2216

7a. NAME OF MONITORING ORGANIZATION

U. S. Army Research Office

7b. ADDRESS (City, State, and ZIP Code)

P. O. Box 12211
Research Triangle Park, NC 27709-22118a. NAME OF FUNDING/SPONSORING
ORGANIZATION

U. S. Army Research Office

8b. OFFICE SYMBOL
(If applicable)

9. PROCUREMENT INSTRUMENT IDENTIFICATION NUMBER

DAAG29-85-C-0002

8c. ADDRESS (City, State, and ZIP Code)

P. O. Box 12211
Research Triangle Park, NC 27709-2211

10. SOURCE OF FUNDING NUMBERS

PROGRAM
ELEMENT NO.PROJECT
NO.TASK
NO.WORK UNIT
ACCESSION NO.

11. TITLE (Include Security Classification)

Navier-Stokes Calculations of Hovering Rotor Flowfields

12. PERSONAL AUTHOR(S)

G. R. Srinivasan and W. J. McCroskey

13a. TYPE OF REPORT
Reprint

13b. TIME COVERED

FROM TO

14. DATE OF REPORT (Year, Month, Day)

15. PAGE COUNT

16. SUPPLEMENTARY NOTATION

The view, opinions and/or findings contained in this report are those of the author(s) and should not be construed as an official Department of the Army position, policy, or decision, unless so designated by other documentation.

17. COSATI CODES

FIELD

GROUP

SUB-GROUP

18. SUBJECT TERMS (Continue on reverse if necessary and identify by block number)

19. ABSTRACT (Continue on reverse if necessary and identify by block number)

ABSTRACT ON REPRINT

Original contains color
plates. All DTIC reproductions
will be in black and white.

20. DISTRIBUTION/AVAILABILITY OF ABSTRACT

☐ UNCLASSIFIED/UNLIMITED ☐ SAME AS RPT ☐ DTIC USERS

21. ABSTRACT SECURITY CLASSIFICATION

Unclassified

22a. NAME OF RESPONSIBLE INDIVIDUAL

22b. TELEPHONE (Include Area Code)

22c. OFFICE SYMBOL

AIAA'87

ARO 21781.4-EG

AIAA-87-2629-CP Navier-Stokes Calculations of Hovering Rotor Flowfields

G. R. Srinivasan,
JAI Associates, Inc., Mountain View, CA
W. J. McCroskey,
U. S. Army Aeroflightdynamics Directorate-AVSCOM,
NASA Ames Research Center, Moffett Field, CA



1. ORDER NO.		
2. ORDER DATE		
3. ORDER BY		
4. ORDER FOR		
5. ORDER BY		
6. ORDER BY		
7. ORDER BY		
8. ORDER BY		
9. ORDER BY		
10. ORDER BY		
11. ORDER BY		
12. ORDER BY		
13. ORDER BY		
14. ORDER BY		
15. ORDER BY		
16. ORDER BY		
17. ORDER BY		
18. ORDER BY		
19. ORDER BY		
20. ORDER BY		
21. ORDER BY		
22. ORDER BY		
23. ORDER BY		
24. ORDER BY		
25. ORDER BY		
26. ORDER BY		
27. ORDER BY		
28. ORDER BY		
29. ORDER BY		
30. ORDER BY		
31. ORDER BY		
32. ORDER BY		
33. ORDER BY		
34. ORDER BY		
35. ORDER BY		
36. ORDER BY		
37. ORDER BY		
38. ORDER BY		
39. ORDER BY		
40. ORDER BY		
41. ORDER BY		
42. ORDER BY		
43. ORDER BY		
44. ORDER BY		
45. ORDER BY		
46. ORDER BY		
47. ORDER BY		
48. ORDER BY		
49. ORDER BY		
50. ORDER BY		
51. ORDER BY		
52. ORDER BY		
53. ORDER BY		
54. ORDER BY		
55. ORDER BY		
56. ORDER BY		
57. ORDER BY		
58. ORDER BY		
59. ORDER BY		
60. ORDER BY		
61. ORDER BY		
62. ORDER BY		
63. ORDER BY		
64. ORDER BY		
65. ORDER BY		
66. ORDER BY		
67. ORDER BY		
68. ORDER BY		
69. ORDER BY		
70. ORDER BY		
71. ORDER BY		
72. ORDER BY		
73. ORDER BY		
74. ORDER BY		
75. ORDER BY		
76. ORDER BY		
77. ORDER BY		
78. ORDER BY		
79. ORDER BY		
80. ORDER BY		
81. ORDER BY		
82. ORDER BY		
83. ORDER BY		
84. ORDER BY		
85. ORDER BY		
86. ORDER BY		
87. ORDER BY		
88. ORDER BY		
89. ORDER BY		
90. ORDER BY		
91. ORDER BY		
92. ORDER BY		
93. ORDER BY		
94. ORDER BY		
95. ORDER BY		
96. ORDER BY		
97. ORDER BY		
98. ORDER BY		
99. ORDER BY		
100. ORDER BY		

AIAA Atmospheric Flight Mechanics Conference

August 17-19, 1987/Monterey, CA

For permission to copy or republish, contact the American Institute of Aeronautics and Astronautics
1633 Broadway, New York, NY 10019

87 9 9 216

NAVIER-STOKES CALCULATIONS OF HOVERING ROTOR FLOWFIELDS

G. R. Srinivasan*

JAI Associates Inc, Mountain View, California

W. J. McCroskey**

U.S. Army Aeroflightdynamics Directorate - AVSCOM
NASA Ames Research Center, Moffett Field, California

Abstract

Unsteady, thin layer Navier-Stokes equations written in rotor coordinates are solved using a partially flux-split, implicit numerical algorithm to calculate the flowfields of a hovering rotor blade at subsonic and transonic conditions. Numerical results are in good agreement with experimental data for both nonlifting and lifting rectangular blades. For the lifting case, the rotor wake effects are modeled by applying a correction to the geometric angle of attack of the blades. Alternate methods of calculating the hovering rotor flowfields in blade-fixed mode that have the same circulation distribution as hovering blade are explored. All of the results presented in this paper are computed on a CRAY2 supercomputer.

Introduction

The need to accurately calculate the flowfield of a helicopter rotor in both hover and forward flight is of great practical importance. Unlike the flowfield of a fixed wing, the flowfield of a helicopter rotor is generally more complex to analyze because it provides some of the most complex challenges to be found in the field of applied aerodynamics. This complexity stems from several peculiar problems that are unique to the helicopter rotor, viz., a radially increasing blade speed that is responsible for a high concentration of bound circulation over the outer portion of the blade resulting in a strong trailed vortex, a spiralling wake vortex sheet remaining initially close to the rotor causing strong blade-vortex interactions, a high centrifugal force field in which the blades operate, a relatively large steady state out-of-plane displacement of the rotor blades and aeroelastic response of the rotor itself, and finally, mutual interaction of flowfields of main rotor, tail rotor and the fuselage. These flowfields are often characterized by transonic conditions and associated shock waves which makes the flow more susceptible to three dimensionality and unsteadiness.

The operating characteristics of such rotary wing vehicles are strongly influenced by the the vortex wake. The interaction of this wake with the following blades is a potential source of noise and vibration at low and moderate flight speeds. Accurate prediction of the vortical wake is probably the most important, most studied and the most difficult aspect of helicopter flowfield. Current methods of

analysis of the wake range in complexity from relatively simple momentum-theory applications to free wake lifting surface methods. In between these extremes, there are a variety of so-called prescribed-wake models, which generally rely on some degree of empiricism to determine the position of the wake vortices; then the Biot-Savart law is used to calculate the induced velocity field due to these vortices at the plane of the rotor blades. Although such models are widely used in current prediction techniques, they suffer from the limitation that the empirical determination of the wake shape ignores some of the important details of the flowfield such as the mutual interaction between various vortex elements. Further, they are unreliable for unusual blade planforms and/or twist distributions which are often the case with modern helicopter blade shapes.

The current thrust in calculating the rotor flowfield more accurately, including the wake effects, is pushing the use of state-of-art computational fluid dynamics (CFD) codes to shed more light on the understanding of this problem. Finite difference codes for nonlinear compressible potential equations (Refs. 1-6) and the Euler equations (Refs. 7-14) have been used to calculate the rotor flowfields. Initially developed methods using the potential flow and the Euler formulations were primarily limited to calculating nonlifting rotor flows because of the inherent limitation of not being able to model the vortex wake with these equations, although the Euler formulation has in it the necessary physics to model vorticity transport correctly. These equations basically lack the physical mechanism needed to generate the vortex wake. However, in conjunction with wake models, such as CAMRAD (Ref. 15) and HOVER (Ref. 16), both potential flow and Euler codes have been used extensively to calculate the lifting rotor flowfields. The standard experimental data that is used in validating most of these codes has been the two-bladed rotor data of Caradonna and Tung (Ref. 17). An excellent review of some of the currently available inviscid finite-difference numerical methods has been presented by Caradonna and Tung in Ref. 18.

As mentioned above, tip vortices are an important part of the helicopter rotor flow field. These vortices, which are generated at the tips of the rotating blades, along with the helical wake vortex sheet have tremendous influence on the operating characteristics of the rotor. Some of the common practical problems caused by such concentrated trailing vortices are the rotor vibration due to unsteady

* Senior Research Scientist, Member AIAA

** Senior Staff Scientist, Associate Fellow AIAA

This paper is declared a work of the U. S. Government and therefore is in the public domain.

lift fluctuation, increased induced drag and the annoying 'blade-slap', an impulsive noise characteristic are a few to name. Many studies have been made to date to understand and reduce the influence of tip vortices by means of modifications to the tip geometry of the rotating blades. Various analytical and numerical studies conducted are basically inviscid in nature and therefore preclude the mechanics of the physics necessary to model correctly the formation of the tip vortex which involves the the complex three-dimensional viscous flowfield in the tip region. The thin layer Navier-Stokes simulations of tip-flows have been attempted only recently after bigger and faster supercomputers became available. The studies of Mansour (Ref. 19) and Srinivasan et al (Ref. 20) show limited success in simulating the complex tip flows. Simulation of the complete vortex wake now appears possible with proper Navier-Stokes algorithm in conjunction with patched and/or zonal grid topology to discretize the flowfield. Understanding the mechanism of the formation process of the tip vortex and its subsequent roll-up would provide a proper insight to modify these tip flows and alleviate some of the problems caused by them. The ability to preserve the concentrated vortices in the finite difference grid without numerical diffusion (Ref. 21) has been the biggest set back until now for much progress in this area. Even the most advanced computational techniques, that use spatial central differencing, lack proper mechanism to preserve concentrated tip vortices and convect them in the flowfield without numerical diffusion. However, the recently developed upwind schemes in conjunction with a proper grid choice appear very promising to preserve and convect concentrated vortices. Alternatively, if the properly captured tip vortex is analytically represented, then prescribed vortex methods (Refs. 22-23) could be applied to calculate the vortex wake development for several rotations of the blade. These methods have demonstrated the ability to preserve and convect concentrated vortices even in very coarse grid regions without significant numerical diffusion.

The use of Navier-Stokes codes to model the rotor flowfields have been limited in the past primarily because of the large computer memory and CPU time requirements. In fact, these codes may not be very much more expensive to run than some of the Euler codes, but to have a meaningful flow definition in the tip region and in the wake might make such a procedure very expensive. Recently, Wake and Sankar (Ref. 24) have presented some nonlifting and lifting calculations for a rotor in hover using a coarse grid with a poor definition of the tip region. The results for surface pressure are in fair agreement with experimental data. The lifting calculations used a correction to the geometric angle of attack of the blade obtained from the lifting surface code of Ref. 16. In the present study, using a good definition of the tip region, thin-layer Navier-Stokes equations are solved for the flowfield of a rectangular blade in hover with a view to capture the tip vortex also. Both nonlifting and lifting cases have been calculated with subcritical and supercritical tip Mach numbers. Surface pressure distributions and tip flow data are presented and compared with experimental data. Alternate methods of calculating the hover flowfield in a non-hover mode (like an isolated

fixed blade), keeping the circulation distribution the same as that of a hovering blade, are explored and the results for these are compared with the hover results. Governing equations and numerical method are presented in the next section followed by results and concluding remarks.

Governing Equations and Numerical Scheme

The governing partial differential equations are the unsteady, thin-layer Navier-Stokes equations. For generality, these equations are transformed from the Cartesian reference frame to the arbitrary curvilinear space (ξ, η, ζ, τ) while retaining strong conservation law-form to capture shock waves. The transformed equations are given by (Ref. 25)

$$\partial_\tau \hat{Q} + \partial_\xi \hat{E} + \partial_\eta \hat{F} + \partial_\zeta \hat{G} = Re^{-1} \partial_\zeta \hat{S} \quad (1)$$

where

$$\hat{Q} = J^{-1} \begin{bmatrix} \rho \\ \rho u \\ \rho v \\ \rho w \\ e \end{bmatrix}, \quad \hat{E} = J^{-1} \begin{bmatrix} \rho U \\ \rho u U + \xi_x p \\ \rho v U + \xi_y p \\ \rho w U + \xi_z p \\ U(e + p) - \xi_t p \end{bmatrix}$$

$$\hat{F} = J^{-1} \begin{bmatrix} \rho V \\ \rho u V + \eta_x p \\ \rho v V + \eta_y p \\ \rho w V + \eta_z p \\ V(e + p) - \eta_t p \end{bmatrix}, \quad \hat{G} = J^{-1} \begin{bmatrix} \rho W \\ \rho u W + \zeta_x p \\ \rho v W + \zeta_y p \\ \rho w W + \zeta_z p \\ W(e + p) - \zeta_t p \end{bmatrix} \quad (2)$$

The viscous flux vector \hat{S} , written here in the limit of thin-layer approximation, is given by

$$\hat{S} = J^{-1} \begin{bmatrix} 0 \\ K_1 u_\zeta + K_2 \zeta_x \\ K_1 v_\zeta + K_2 \zeta_y \\ K_1 w_\zeta + K_2 \zeta_z \\ K_1 (Pr^{-1}(\gamma - 1)^{-1}(a^2)_\zeta + ((q^2)/2)_\zeta) + K_2 K_3 \end{bmatrix} \quad (3)$$

where

$$K_1 = \mu(\zeta_x^2 + \zeta_y^2 + \zeta_z^2)$$

$$K_2 = \mu(\zeta_x u_\zeta + \zeta_y v_\zeta + \zeta_z w_\zeta)/3$$

$$K_3 = u \zeta_x + v \zeta_y + w \zeta_z$$

$$q^2 = u^2 + v^2 + w^2 \quad (4)$$

The primitive variables of Eq. (1), viz., the density ρ , the mass fluxes $\rho u, \rho v, \rho w$ and the energy per unit volume e , are normalized by the free-stream reference quantities. The reference length and velocity scales are the chord of the rotor blade and free stream speed of sound respectively. Other nondimensional quantities appearing in the above equations are the Reynolds number Re and the Prandtl

number Pr ; μ is the dynamic viscosity. The relations for the contravariant velocities U , V and W , the Jacobian of transformation J , and the metrics of the transformation $(\xi_t, \xi_x, \xi_y, \xi_z)$, $(\eta_t, \eta_x, \eta_y, \eta_z)$ and $(\zeta_t, \zeta_x, \zeta_y, \zeta_z)$ can be found in Ref. 25.

The velocity components u, v, w and the pressure, p , are related to the total energy per unit volume, e , through the equation of state for a perfect gas by

$$p = (\gamma - 1)(e - \frac{\rho}{2}(u^2 + v^2 + w^2)) \quad (5)$$

where γ is the ratio of specific heats.

In the above equations u, v , and w are the Cartesian components of the velocity in the inertial coordinate system (x, y, z, t) . In the present formulation Eq. (1) is solved in the inertial frame of reference. The inertial coordinates $\bar{X} = (x, y, z, t)$ are related to the blade fixed coordinates $\bar{X}_b = (\bar{x}, \bar{y}, \bar{z}, \bar{t})$ through the relation given by

$$\bar{X}(x, y, z) = \mathbf{R}(t)\bar{X}_b(\bar{x}, \bar{y}, \bar{z}) \quad (6)$$

$$t = \bar{t}$$

where $\mathbf{R}(t)$ is the rotational matrix (Ref. 26) given by

$$\mathbf{R}(t) = \begin{bmatrix} \cos \Omega \bar{t} & -\sin \Omega \bar{t} & 0 \\ \sin \Omega \bar{t} & \cos \Omega \bar{t} & 0 \\ 0 & 0 & 1 \end{bmatrix} \quad (7)$$

Here Ω is the reduced frequency of the rotor and $\Omega \bar{t}$ represents the azimuth sweep of the rotor blade. In view of this relation, Eq. 7, the metrics in inertial reference frame are related to those in the blade-fixed frame of reference through

$$\begin{aligned} \xi_x &= \xi_{\bar{x}} \cos \Omega \bar{t} - \xi_{\bar{y}} \sin \Omega \bar{t} \\ \xi_y &= \xi_{\bar{x}} \sin \Omega \bar{t} + \xi_{\bar{y}} \cos \Omega \bar{t} \\ \xi_z &= \xi_{\bar{z}} \\ \eta_x &= \eta_{\bar{x}} \cos \Omega \bar{t} - \eta_{\bar{y}} \sin \Omega \bar{t} \\ \eta_y &= \eta_{\bar{x}} \sin \Omega \bar{t} + \eta_{\bar{y}} \cos \Omega \bar{t} \\ \eta_z &= \eta_{\bar{z}} \\ \zeta_x &= \zeta_{\bar{x}} \cos \Omega \bar{t} - \zeta_{\bar{y}} \sin \Omega \bar{t} \\ \zeta_y &= \zeta_{\bar{x}} \sin \Omega \bar{t} + \zeta_{\bar{y}} \cos \Omega \bar{t} \\ \zeta_z &= \zeta_{\bar{z}} \\ \xi_t &= \Omega \bar{y} \xi_{\bar{x}} - \Omega \bar{x} \xi_{\bar{y}} \\ \eta_t &= \Omega \bar{y} \eta_{\bar{x}} - \Omega \bar{x} \eta_{\bar{y}} \\ \zeta_t &= \Omega \bar{y} \zeta_{\bar{x}} - \Omega \bar{x} \zeta_{\bar{y}} \end{aligned} \quad (8)$$

The equations set, Eq. 1, is solved using an implicit, approximately-factored numerical scheme that uses spatial central differencing in the η and ζ directions and upwind differencing in the ξ direction developed by Ying et al (Ref. 27). The flux vector \hat{F} has been split in to \hat{F}^+ and \hat{F}^- according to its eigenvalues. Artificial dissipation terms (second- and fourth-order) have been added in the central differencing directions for stability reasons (see Ref. 25). The factored operators can be solved by sweeping in

the ξ direction and inverting tridiagonal matrices with 5 x 5 blocks for the other two directions. Currently, significant part of the computational time is taken to form the plus and minus Jacobian matrices for the flux vector \hat{F} with this numerical scheme. The numerical code is vectorized for the CRAY2 supercomputer.

A body conforming finite-difference grid has been used for the rectangular blade having a rounded-tip cap and consists of warped spherical O-O grid topology. The flowfield grid is numerically generated using the three-dimensional hyperbolic grid solver of Steger and Chaussee (Ref. 28) with proper clustering in the leading and trailing edge regions and in the tip region. The grid is nearly orthogonal at the surface and the spacing in the normal direction at the surface is chosen to be 0.00006 of the chord. All the computations were done with one grid topology having 155 points in the periodic direction around the airfoil, and 66 points each in the spanwise and normal directions, for a total of about 700,000 grid points. The grid boundary is chosen to be at 10 chords in all directions.

The boundary conditions consist of surface boundary conditions and farfield boundary conditions and are applied explicitly. For the nonrotating blade the noslip condition is enforced at the wall by setting U , V and W to be zero and ξ_t , η_t and ζ_t are zero as the grid is stationary. For the rotating blade, however, U , V and W are still set to zero but ξ_t , η_t and ζ_t are nonzero as the blade (and the grid attached to it) is moving in azimuth. Also, at the wall the density is determined by assuming adiabatic wall condition. The pressure along the body surface is calculated from the normal momentum relation (see for example Ref. 25). Having known the density and pressure, the total energy is determined from the equation of state.

At the farfield boundary the flow quantities are either fixed or extrapolated from the interior depending on whether the flow is subsonic or supersonic and if it is of inflow- or outflow-type at the boundary. The characteristic velocities of the Euler equations determine the number of flow properties to be specified to control the reflections of waves from the boundaries. For subsonic-inflow boundary, four quantities must be specified. Thus density is extrapolated while the velocities and the total energy are specified by the free stream values. For supersonic-inflow, all flow quantities are specified. At subsonic-outflow boundaries, only one quantity is specified, viz., pressure is fixed. For supersonic-outflow condition all flow quantities are extrapolated from the interior. At the plane containing the blade root $\partial Q / \partial y = 0$ is imposed.

Results and Discussion

Both time accurate and time asymptotic (steady state) calculations are performed in this study for an aspect ratio 6 rectangular blade having no twist or taper. The blade, which has a round tip-cap (body of revolution), is made up of NACA0012 airfoil section. The rotating blade calculations presented here have been chosen to correspond to the experimental test conditions of a two-bladed hovering rotor of Caradonna and Tung (Ref. 17). At the

Reynolds number corresponding to the tip speeds in this test, the boundary layer can be assumed to be turbulent over the entire blade and Baldwin and Lomax algebraic turbulence model (Ref. 29) is used to calculate the turbulent eddy viscosity. A typical solution, with vectorized code for CRAY2, required about 700-1000 marching steps (approximately 45-60 degrees of azimuth travel) to reach quasi-steady flow conditions with CPU time per time step per grid point of 8.5×10^{-5} sec. Time accurate calculations were run with a maximum value for the time step of $\Delta t = 0.01$, whereas the fixed blade option used variable time step option (Ref. 21) with Δt of 5 to calculate steady state flowfield.

Hovering Blade

As mentioned before, the rotating blade calculations presented here correspond to the two-bladed hover test conditions of Caradonna and Tung (Ref. 17). Hover calculations have been done in a time accurate fashion. In practice, a hovering rotor flowfield is quasi-steady in blade-fixed coordinates system. Since the governing equations are being solved in the inertial reference frame in the present approach, the flowfield never reaches steady state in this reference frame. This approach was preferred since it is easily extendable to the forward flight case.

Figure 1 shows the chordwise surface pressure distributions at several radial stations for the nonlifting rotor with tip Mach number $M_{tip} = 0.52$ and a corresponding Reynolds number of 2.32 million. As seen, the calculated results are in excellent agreement with experimental data at all radial stations. Accurate calculation of lifting rotor flowfields is possible only if the induced effects of the wake are properly included in the analysis. At present a number of methods are available to model the effects of the wake of a hovering rotor. All these methods seem to give approximately the same kind of results when applied to a particular problem, not dominated by viscous effects, as is shown in the review of Caradonna and Tung (Ref. 18). With this observation, a uniform correction to the angle of attack of the blade has been made in this study based on the estimates of induced downwash for the experimental test rotor configuration given by Agarwal and Deese (Ref. 11). Figure 2, reproduced from Ref. 11, shows plots of sectional induced velocity estimated from a free-wake analysis program for three speeds of rotor and thrust coefficients of an experimental configuration. Over a section of the blade, approximately from 0.4 to 0.9 radius in this figure, the induced downwash given by the ratio of sectional induced velocity to the local blade speed is nearly constant equal to -3.8 degrees for the entire range of test conditions. In the present calculations this induced downwash is chosen as a representative value and is assumed constant for the entire blade.

The effective pitch of the hovering blade is then the difference of the geometric angle of attack and the induced downwash estimated above. Using this estimate, lifting calculations have been performed for hovering blades set at an effective pitch of 4.2 degrees and having tip Mach numbers of 0.44 and 0.877, respectively. Figures 3 and 4 show the

computed results for these cases in the form of surface pressure distributions for representative blade radial stations compared with the experimental data of Caradonna and Tung (Ref. 17). The comparison shows very good agreement, at least for the radial stations between 0.6 to 0.95 of radius, for both subcritical and supercritical cases. The agreement progressively deteriorates for radial stations less than 0.6R which probably is expected from the data for Fig. 2. Agarwal and Deese (Ref. 11) also calculated the same flow using the finite volume Euler formulation and the same induced downwash correction. They also get similar agreement with the experimental data for the subcritical case. However, the shock locations are over estimated for supercritical case in their calculations.

Additional flowfield data for the tip region are presented in Figs. 5-10 for the two lifting cases calculated here. It is well known that the formation of tip vortex involves complex three-dimensional flow separation in the tip region as a necessary condition. Figure 5a shows a view of the surface particle flow traces in the tip region for the subcritical lifting configuration corresponding to a tip Mach number of $M_{tip} = 0.44$. It is generated by releasing fluid particle tracers at one grid point above the surface and confining the flow to stay in that plane. This view is supposed to mimic the surface oil flow pattern often used in laboratory experiments. The separation and reattachment lines of the flow are marked by the symbols *S* and *R* respectively in Fig. 5a. The extent of separation on the upper surface, inboard of tip, is much larger compared to the mild separation seen on the lower surface of the tip region. The braiding of flow particle tracers, released from different locations on the upper and lower surfaces, in the tip region show the formation process of tip vortex in Fig. 6a. In contrast to a nonrotating blade (Ref. 20), the braiding of particle tracers from upper and lower surfaces is delayed until after the vortex lifts-off from the surface. The initial braiding process is comprised of mostly the particles from the upper surface as is clearly seen in Fig. 6a. The strength of the vortex is determined, as before (Ref. 20), by the line integral of the velocity vector over a closed path enclosing the vortex. Estimations done at several locations in the downstream wake by this method gave a value of 0.08 to 0.09 depending on the size of the line integral path chosen for the vortex strength. The integrated lift from the blade pressure distributions was found to be 0.19. The vorticity contours shown in Fig. 6a show the size and shape of the tip vortex. As expected, the coarse grid has smeared-off the tightly wound vortex as seen in this figure.

Similar results are presented for the lifting hovering rotor blade with $M_{tip} = 0.877$ in Figs. 7-10. The pressure contours of Fig. 7a show the extent of transonic flow and steeping of the shock wave towards the tip region. The surface particle flow pattern of Fig. 8a clearly identify the regions of separation and reattachment. As before, the separation seen on the lower surface in the tip region is milder compared to the extent seen inboard of the upper surface. The formation process of the tip vortex, seen in Fig. 9a, shows the braiding of particle tracers initially consisting mostly from the upper surface before lifting-off

the upper surface inboard of the tip. Further braiding of this from the particles from the lower surface occurs in the wake during the roll-up process. The view looking at the tip, seen in Fig. 9a, clearly shows the lifting-off of the tip vortex from the separated region on the upper surface. A farfield view of this vortex is shown in Fig. 10a. The vorticity contours shown in this figure at different x-locations in the wake suggests approximate shape of the vortex. The strength of this vortex estimated, as before, gave a value of 0.07-0.08. The integrated value of the lift coefficient for this case is 0.17.

Fixed Blade

The results presented in the above section for the hovering blade were computed in a time accurate manner as mentioned before and these are time consuming and expensive. So this section explores alternate methods to compute the quasi-steady flowfield of the hovering rotor, in particular, as flowfield of a fixed blade with the same circulation distribution as that of the hovering rotor blade with the same tip Mach number. Comparing the circulation distribution for these two modes (fixed and rotating blade), one can immediately come up with two different ways of generating approximately the same circulation distribution on a fixed blade as that of the hovering blade keeping the planform of the blade same by a) having the flow Mach number distributed as a function of the radial distance exactly like a hovering blade, keeping every thing else same, and b) alternatively keeping the flow Mach number uniform for the entire blade equal to the tip speed and then have a twist distribution along the blade which decreases from the tip to the root of the blade. This means that the fixed blade will have variable twist increasing towards the tip to a value equal to the value of effective pitch of the hovering blade. A third option, that of increasing the chord linearly from the root to the tip, was not explored in this investigation.

With the above reasoning, steady state flowfields were calculated just like a fixed isolated blade flowfield with the free stream conditions as discussed above. These calculations used variable time step option suggested in Ref. 21. Figures 11 and 12 show these results in the form of surface pressure distributions compared with the hovering rotor results for both subcritical and supercritical cases. The subcritical results presented in Fig. 11 show surprisingly very good agreement with the hover results for both the options of variable twist and variable Mach number. Considering close agreement of the results even at the radial station near the tip of the blade, the influence of the centrifugal forces present in rotating blade seem to have very little influence in modifying the pressure field in the tip region. There are very small differences in the surface particle flow patterns and the locations of vortex lift-off from the surface for these cases compared to the hovering blade as seen in Figs. 6 and 7. The fixed-blade configurations seem to produce tightly wound vortex even before leaving the blade, but its strength appears to be within 5-10 percent of the hovering blade value.

The supercritical results, presented in Fig. 12, although dominated by the transonic shocks in the tip region

show very good agreement of the variable Mach number case with the hover case. The variable twist option does not seem to perform as well in the transonic regime. This is not surprising since high flow Mach number (equal to tip Mach number of rotor) exists all along the span for this non-rotating case. Figures 7b and 7c show the upper surface pressure contour plots for these cases and comparing these with that of hovering blade in Fig. 7a demonstrates the closeness of the variable Mach number fixed-blade case with the hovering case. The variable twist case produces too strong a shock wave along the entire blade with the consequence of producing a totally different flowfield. The close agreement of the flowfield for the cases of Figs. 7a and 7b suggests that even at this supercritical flow condition, the influence of the centrifugal forces appear to have minimal overall effect on the flowfield. However, the surface particle flow pattern seen in Figs. 8a-8c shows differences in the flowfields in the tip region for these cases. The rotating-blade case of Fig. 8a and the fixed-blade case of Fig. 8b although have similar surface pressure distributions, the flow in the tip region near the surface appear different. The difference between the two cases should come from the difference in these force fields, which means that the presence of centrifugal force in the rotating-blade case may have produced a small-scale local separation on the lower surface of the tip in addition to the separation seen on the upper surface of the blade. This separation is clearly seen in Fig. 8a. The flow in the tip region for the fixed-blade cases of Figs. 8b and 8c are largely similar even though the flowfield for the case of Fig. 8c is dominated by the strong shock wave and its associated effects. However, the nearfield views of the tip vortices shown in Figs. 9a-9c appear nearly identical, although the lift-off of the tip vortex for hovering blade occurs well inboard of the tip on the upper surface in contrast to the fixed blade cases of Figs. 9b and 9c for which the lift-off appear to occur right in the tip region on the upper surface of the blade. The farfield views of the tip vortices for these cases is shown in Figs. 10a-10c along with vorticity contours insert showing the cross sections of the tip vortices and approximate shapes at various distances from the blade. While the strength of the tip vortex for the variable Mach number case is almost identical to that of the hovering blade case, the variable twist case produced a vortex approximately 2.5 times that of the hovering case. The vortex shapes, determined by the vorticity contour inserts, appear to be same for all cases. It should be emphasised again that these time accurate and steady state calculations were done on the same grid topology to remove the grid dependency from the comparisons.

Conclusions

Unsteady, thin layer Navier-Stokes equations written in rotor coordinates are solved using a flux-split approximately factored, implicit, numerical algorithm to calculate the quasi-steady flowfield of a hovering rotor blade. The test cases chosen correspond to the experimental model hover test conditions of Caradonna and Tung (Ref. 17). The numerical results compare very well with the experimental data for both nonlifting and lifting cases. The induced wake effects in the lifting calculations were accounted as a correction to the geometric angle of attack (pitch). Al-

ternate methods are explored to calculate the hovering rotor flowfield as steady state flowfield on fixed isolated blade keeping the same circulation distribution as that of the hovering blade. Of the two options considered, the variable free stream Mach number case gave almost identical results as that of a rotor at both subcritical and supercritical flow conditions. The variable twist option, on the other hand, gave similar results only under subcritical flow conditions; the supercritical flow condition was dominated by strong transonic shocks. Under conditions where the fixed blade flowfield closely agreed with that of hovering blade, the influence of the centrifugal forces of the rotating blade appeared to have minimum influence on the overall flowfield properties. While these conclusions are preliminary and primarily based on the comparison of surface pressures and vortex strength estimates, further quantitative comparison of the vortex structure is needed for a clear understanding of the similarities and differences.

Acknowledgements

The first author would like to acknowledge the support of this research by the U. S. Army Research Office under Contract DAAG29-85-C-0002 with Dr. R. E. Singleton as the Technical Monitor. Computational support is provided by Dr. T. L. Holst, Chief of Applied Computational Fluids Branch at NASA Ames Research Center. The authors would like to thank Dr. J. L. Steger for many helpful discussions. The graphics work presented here was generated using PLOT3D program developed by Dr. P. G. Buning at NASA Ames Research Center.

References

1. Caradonna, F. X. and Isom, M. P., "Subsonic and Transonic Potential Flow over Helicopter Rotor Blades", AIAA Journal, Vol. 10, No. 12, December 1972, pp. 1606-1612.
2. Chang, I.-C., "Transonic Flow Analysis for Rotors", NASA TP-2375, 1984.
3. Strawn, R. C. and Caradonna, F. X., "Conservative Full-Potential Model for Unsteady Transonic Rotor Flows", AIAA Journal, Vol. 25, No. 2, February 1987, pp. 193-198.
4. Steinhoff J. and Ramachandran, K. "Free Wake Analysis of Compressible Rotor Flows", AIAA Paper No. AIAA-87-0542, January 1987, Reno, Nevada.
5. Strawn, R. C. and Tung, C., "The Prediction of Transonic Loading on Advancing Helicopter Rotors", Paper presented at the AGARD/FDP Symposium on Applications of Computational Fluid Dynamics in Aeronautics, France, April 1986.
6. Strawn, R. C. and Tung, C., "Prediction of Unsteady Transonic Rotor Loads with a Full-Potential Rotor Code", Paper presented at the 43rd Annual Forum of American Helicopter Society, May 1987, St. Louis, Missouri.
7. Wake, B. E., Sankar, N. L. and Lekoudis, S. G., "Computation of Rotor Blade Flows using the Euler Equations", Journal of Aircraft, Vol. 23, No. 7, July 1986, pp. 582-588.
8. Chen, C.-L., McCroskey, W. J. and Ying, S. X., "Euler Solution of Multi- Blade Rotor Flow", Paper to be presented at the 13th European Rotorcraft Forum, France, September 1987.
9. Roberts, T. W. and Murman, E. M., "Solution Method for a Hovering Helicopter Rotor using the Euler Equations", AIAA Paper No. AIAA-85-0436, January 1985, Reno, Nevada.
10. Kroll, N., "Computations of the Flow Fields of Propellers and Hovering Rotors using Euler Equations", Paper No. 28, 12th European Rotorcraft Forum, Federal Republic of Germany, September 1986.
11. Agarwal, R. K. and Deese, J. E., "Euler Calculations for Flowfield of a Helicopter Rotor in Hover", AIAA Paper No. AIAA-86-1782, June 1986, San Diego, California.
12. Sankar, N. L. and Tung, C., "Euler Calculations for Rotor Configurations in Unsteady Forward Flight", Proceedings of the 42nd Annual Forum of American Helicopter Society, June 1986, Washington, D. C., pp. 985-995.
13. Chang, I.-C. and Tung, C., "Euler Solution of the Transonic Flow for a Helicopter Rotor", AIAA Paper No. AIAA-87-0523, January, Reno, Nevada.
14. Agarwal, R. K. and Deese, J. E., "An Euler Solver for Calculating the Flowfield of a Helicopter Rotor in Hover and Forward Flight", AIAA Paper No. AIAA-87-1427, June 1987, Honolulu, Hawaii.
15. Johnson, W., "A comprehensive Analytical Model of Rotorcraft Aerodynamics. Part 1, Analysis Development", NASA TM-81182, 1980.
16. Summa, J. M. and Clark, D. R., "A Lifting Surface Method for Hover/Climb Loads", Proceedings of the American Helicopter Society 35th Annual Forum, May 1979.
17. Caradonna, F. X. and Tung, C., "Experimental and Analytical Studies of a Model Helicopter Rotor in Hover", NASA TM-81232, September 1981.
18. Caradonna, F. X. and Tung, C., "A Review of Current Finite Difference Rotor Flow Codes", Proceedings of the 42nd Annual Forum of the American Helicopter Society, Washington, D. C., June 1986, pp. 967-983.
19. Mansour N.N., "Numerical Simulation of the Tip Vortex Off a Low-Aspect Ratio Wing at Transonic Speed", AIAA Journal, Vol. 23, No. 8, August 1985, pp. 1143-1149.
20. Srinivasan, G. R., McCroskey, W. J., Baeder, J. D. and Edwards, T. A., "Numerical Simulation of Tip Vortices of Wings in Subsonic and Transonic Flows", AIAA Paper No. AIAA-86-1095, May 1986, Atlanta, Georgia.

21. Srinivasan, G. R., Chyu, W. J., and Steger, J. L., "Computation of Simple Three-Dimensional Wing-Vortex Interaction", AIAA Paper No. AIAA-81-1206, June 1981, Palo Alto, California.
22. Steinhoff, J. and Suryanarayanan, K., "The Treatment of Vortex Sheets in Compressible Potential Flow", AIAA Paper No. AIAA-83-1881-CP, 1983.
23. Srinivasan, G. R. and McCroskey, W. J., "Numerical Simulation of Unsteady Airfoil-Vortex Interactions", VERTICA, Vol. 11, No. 1/2, 1987, pp. 3-28.
24. Wake, B. E. and Sankar, L. N., "Solutions of the Navier-Stokes Equations for the Flow About a Rotor Blade", Proceedings of National Specialists' Meeting on Aerodynamics and Aeroacoustics, February 1987, Arlington, Texas.
25. Pulliam, T. H. and Steger, J. L., "Implicit Finite-Difference Simulations of Three-Dimensional Compressible Flow", AIAA Journal, Vol. 18, No. 2, February 1980, pp. 159-167.
26. Isom, M. P., "Unsteady Subsonic and Transonic Potential Flow over Helicopter Rotor Blades", NASA CR-2463, October 1974.
27. Ying, S. X., Steger, J. L., Schiff, L. B. and Baganoff, D., "Numerical Simulation of Unsteady, Viscous, High-Angle-Of-Attack Flows Using a Partially Flux-Split Algorithm", AIAA Paper No. AIAA-86-2179, AIAA 13th Atmospheric Flight Mechanics Conference, August 1986, Williamsburg, Virginia.
28. Steger, J. L. and Chaussee, D. S., "Generation of Body-Fitted Coordinates Using Hyperbolic Partial Differential Equations", SIAM J. Sci. Stat. Comput., Vol. 1, No. 4, December 1980, pp. 431-437.
29. Baldwin, B. S. and Lomax, H., "Thin Layer Approximation and Algebraic Model for Separated Turbulent Flow", AIAA Paper No. AIAA-78-257, January 1978, Huntsville, Alabama.

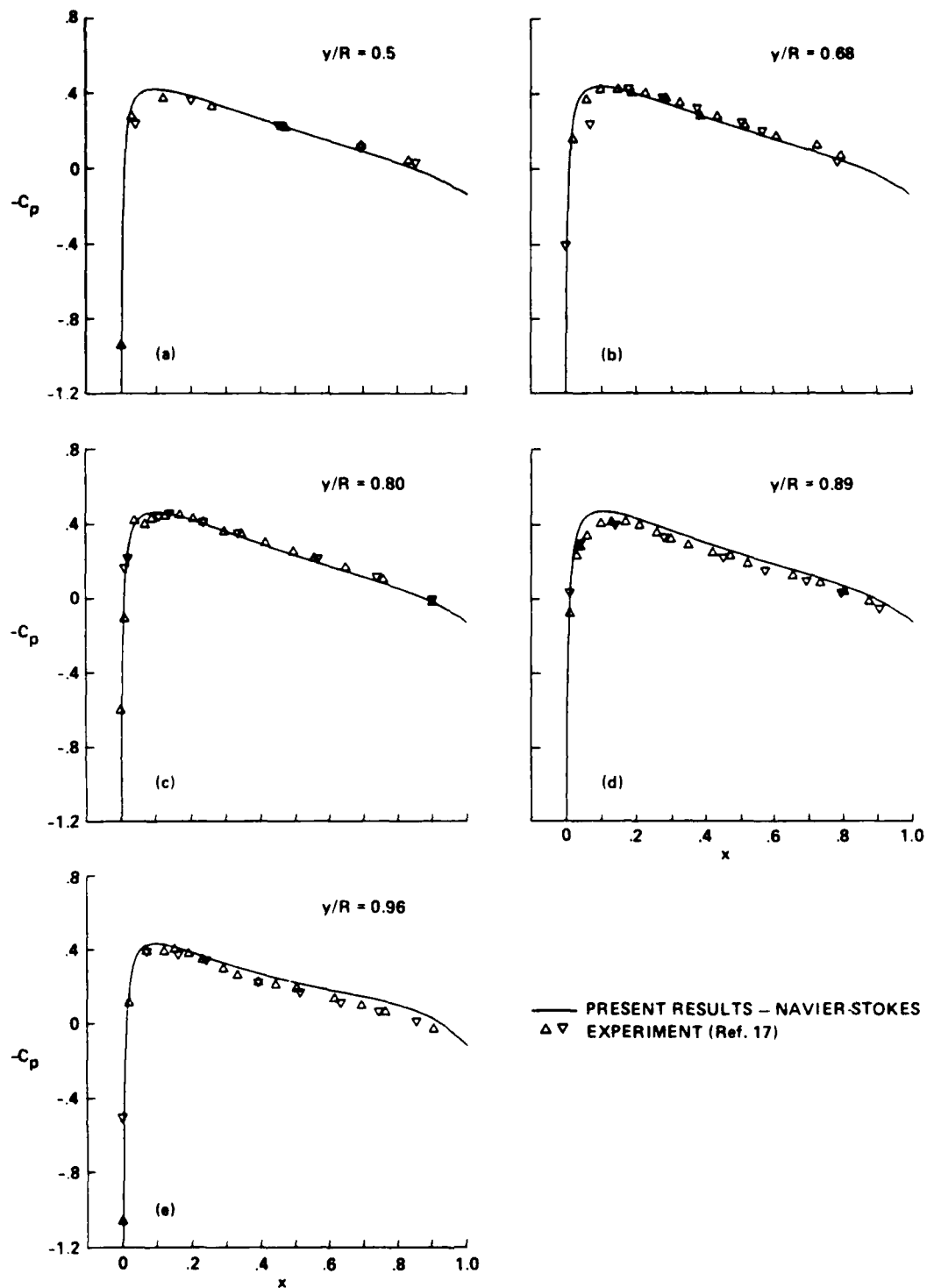


Fig. 1 Surface pressure distributions on a nonlifting rotor in hover;
 $M_{tip} = 0.52$, $Re = 2.32$ million.

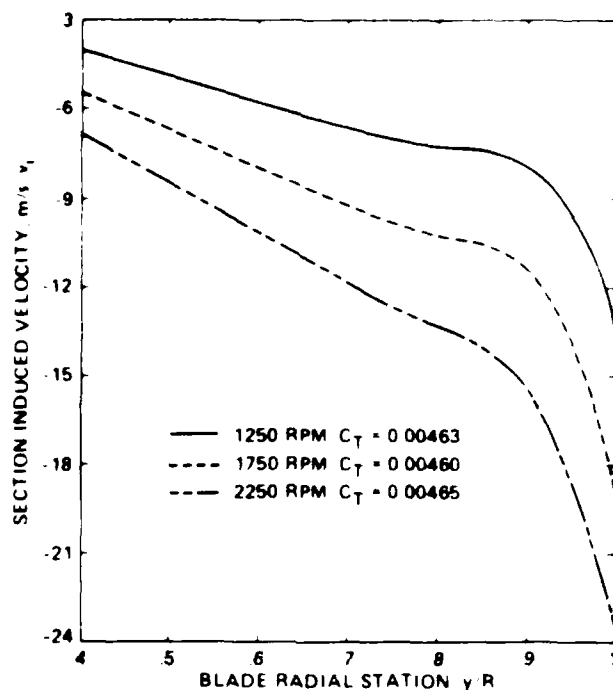


Fig. 2 Wake-induced velocity distribution along the radius of a hovering rotor blade obtained from a Free-Wake Analysis Program. (Figure reproduced from Ref. 11)

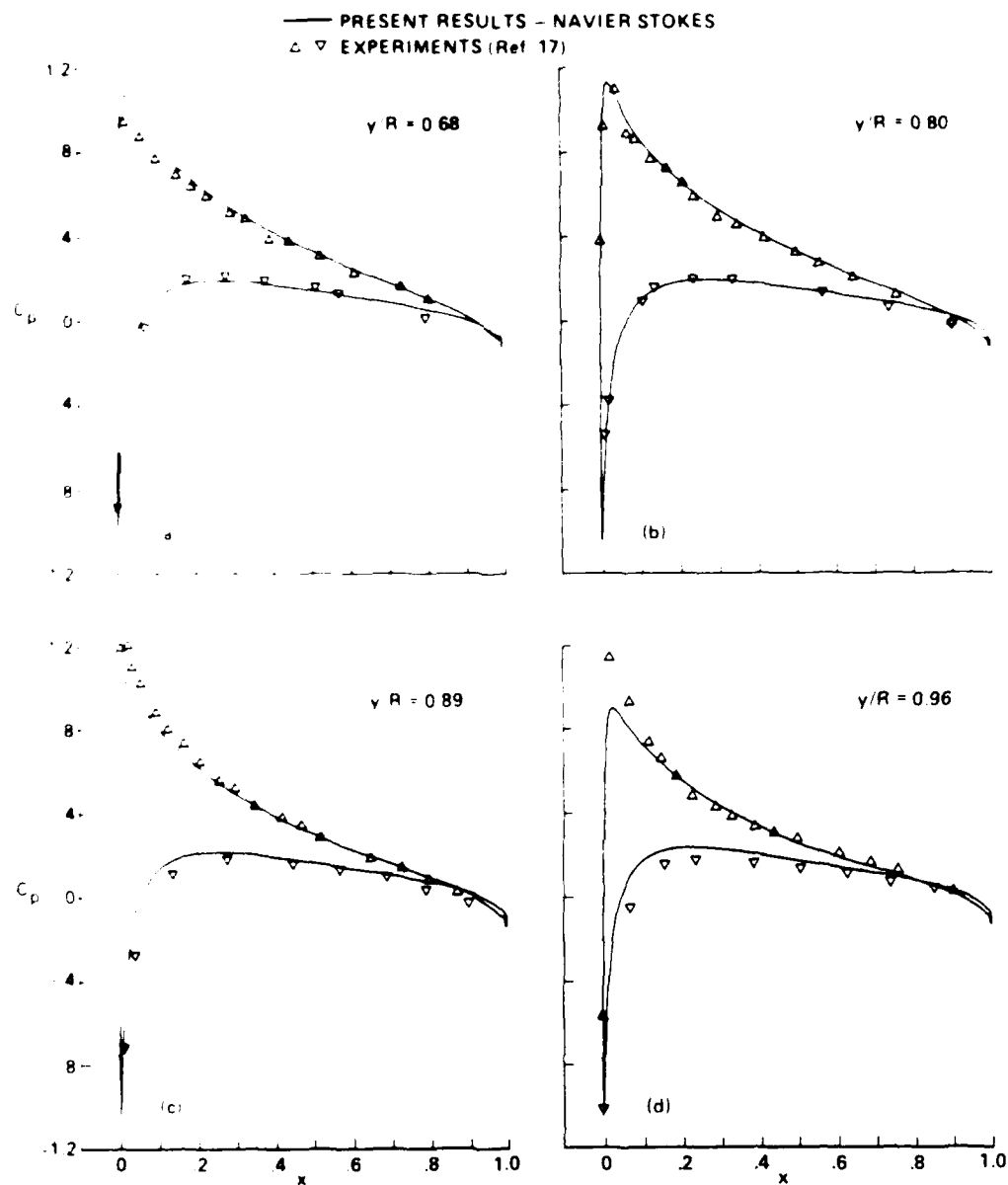


Fig. 3 Surface pressure distributions on a lifting rotor in hover;
 $M_{tip} = 0.44$, Effective pitch = 4.2 deg., $Re = 1.9$ million.

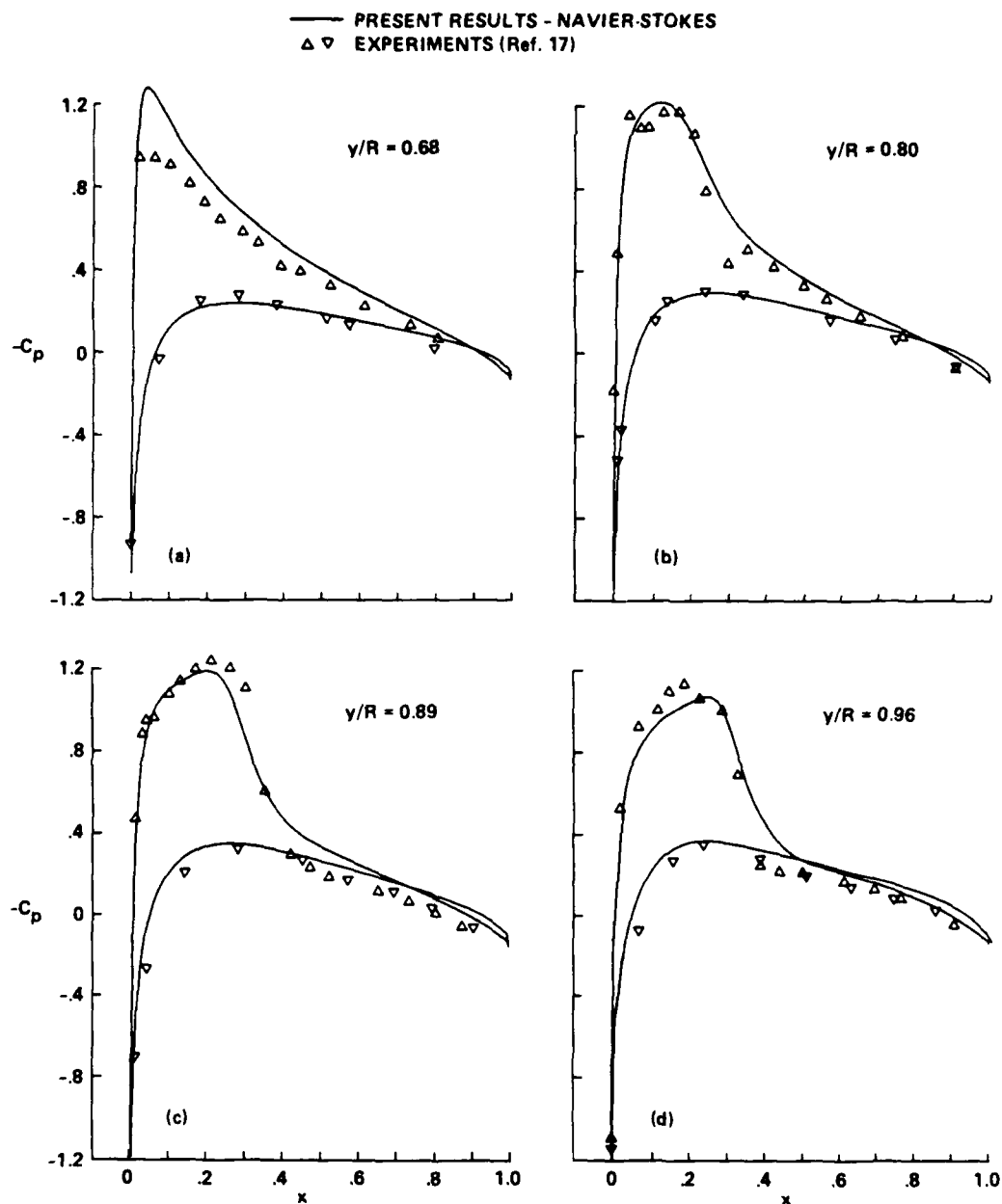
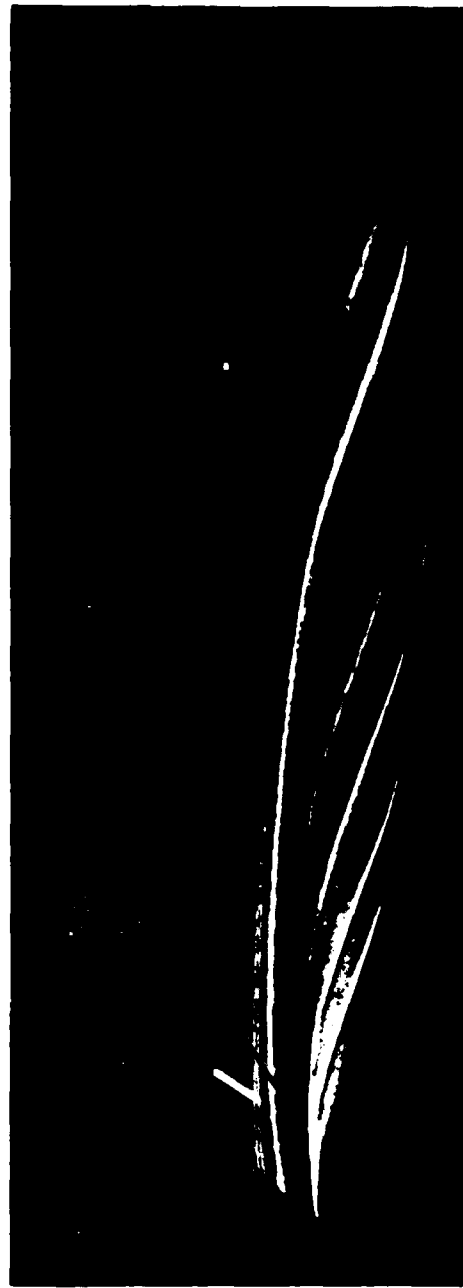


Fig. 4 Surface pressure distributions on a lifting rotor in hover;
 $M_{tip} = 0.877$, Effective pitch = 4.2 deg., $Re = 3.83$ million.



a) ROTATING BLADE



b) FIXED BLADE - $M_{\infty}(y)$

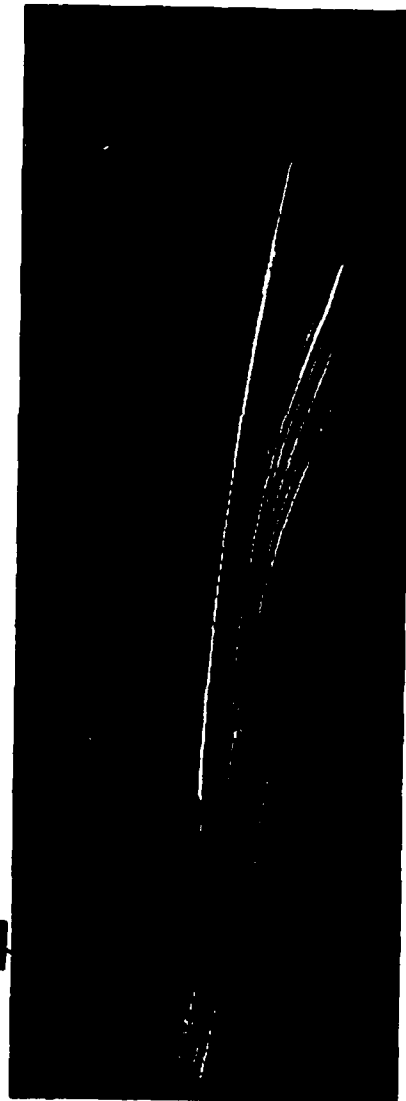
Fig. 5 Surface particle flow traces in the tip region of a lifting rotor blade;
 $M_{\infty} = 0.44$, $Re = 1.92$ million

$x = 4.6$ $x = 0.25$



a) ROTATING BLADE

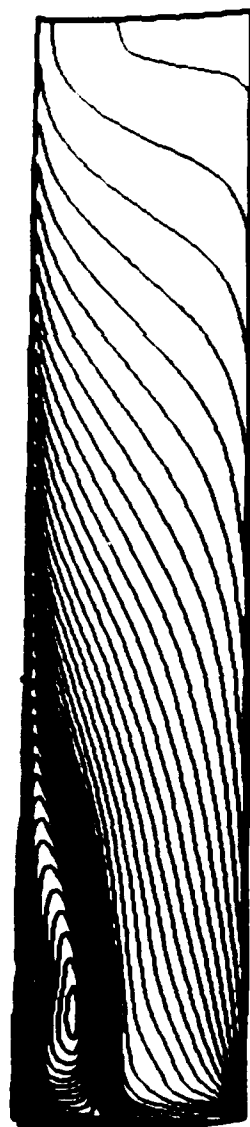
$x = 4.6$



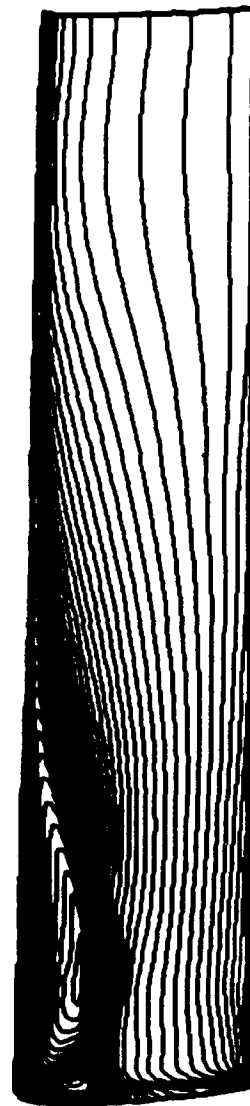
b) FIXED BLADE - $M_\infty(y)$

Fig. 6 View of the tip vortex formation and lift-off from the surface for a lifting rotor blade.

$M_{tip} = 0.44$, $Re = 1.92$ million.



a) ROTATING BLADE



b) FIXED BLADE - VARIABLE MACH NUMBER



c) FIXED BLADE - VARIABLE PITCH (TWISTED)

Fig. 7 Surface pressure contours of a lifting blade; $M_{tip} = 0.877$, $Re = 3.93$ million.



a) ROTATING BLADE



b) FIXED BLADE - $M_{\infty}(y)$



c) FIXED BLADE - $\theta(y)$

Fig. 8 Surface particle flow traces in the tip region of lifting rotor blades;
 $M_{tip} = 0.877$, $Re = 3.93$ million.



a) ROTATING BLADE



b) FIXED BLADE - $M_{\infty}(y)$



c) FIXED BLADE - $\theta(y)$

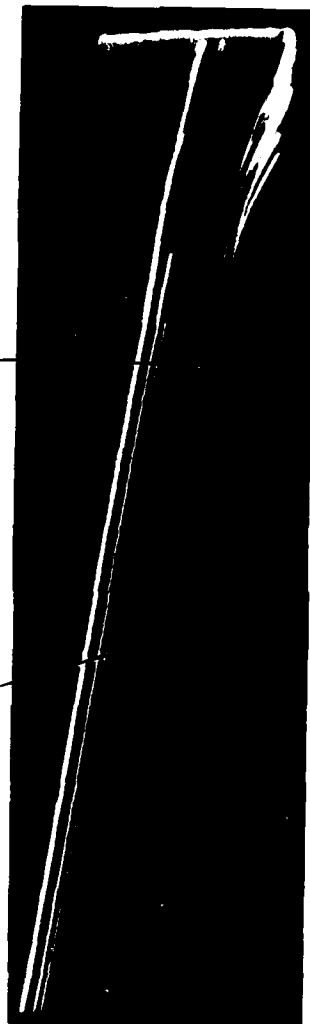
Fig. 9 Near-field view of tip vortex formation and lift-off from the surface of lifting rotor blade: $M_{\infty} = 0.877$, $Re = 3.93$ million.

$x = 4.6$ $x = 1.0$ $x = 0.25$



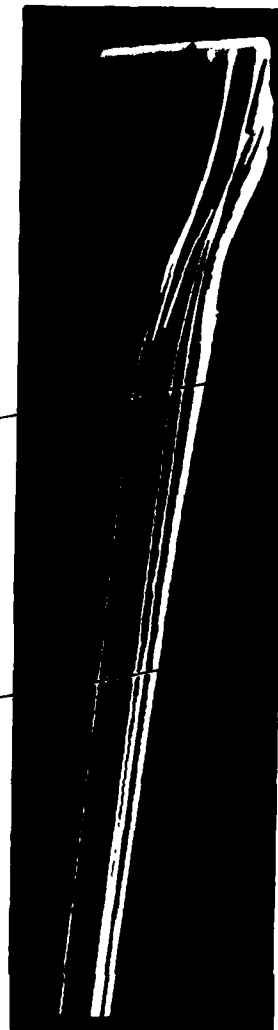
a) ROTATING BLADE

$x = 4.6$ $x = 0.25$



b) FIXED BLADE - $M_{\infty}(y)$

$x = 4.6$ $x = 0.25$



c) FIXED BLADE - $\theta(y)$

Fig. 10 Far-field view of tip vortex showing roll-up in the wake of lifting rotor blade:
 $M_{\infty} = 0.877$, $Re = 3.93$ million.

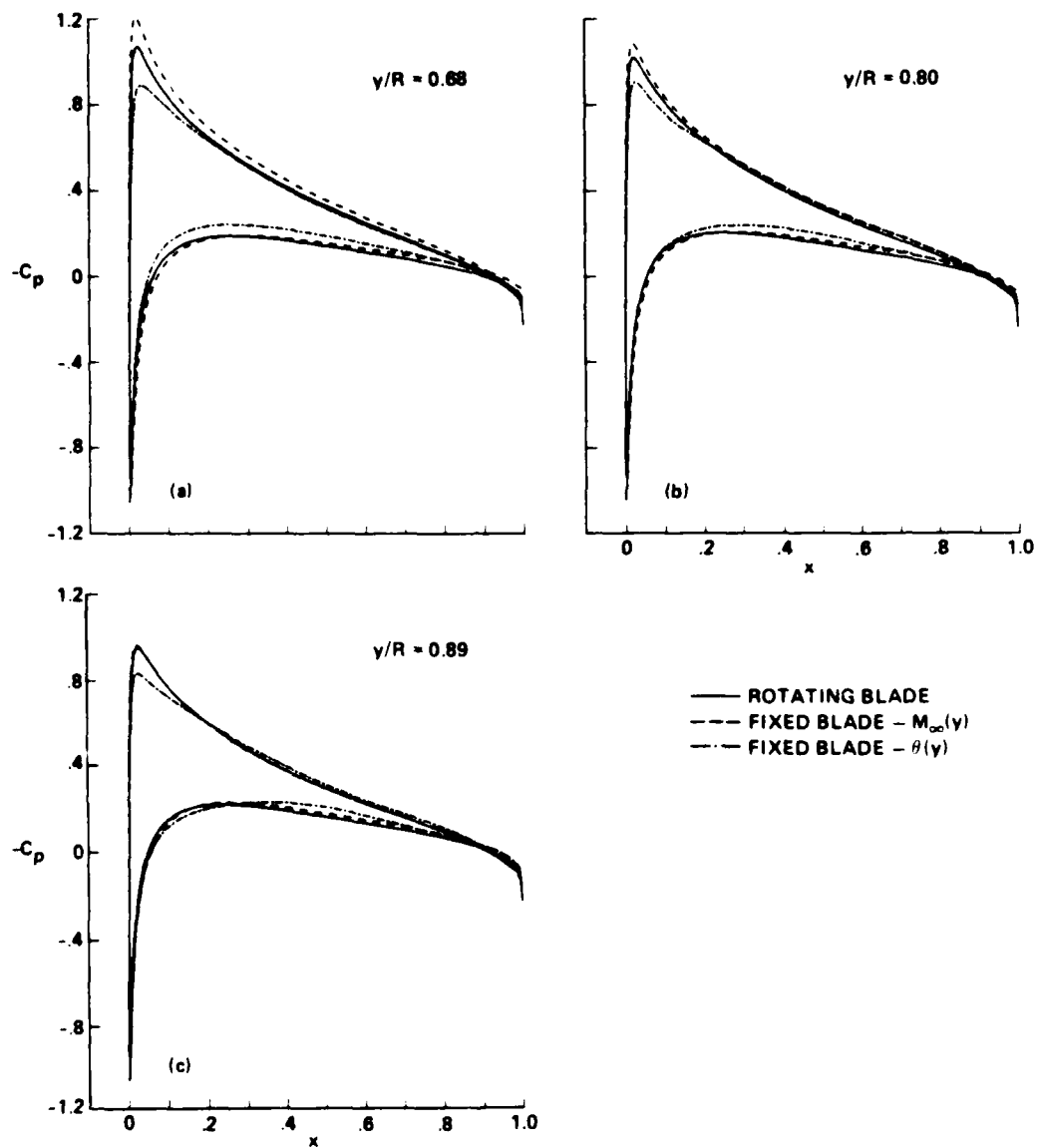


Fig. 11 Comparison of surface pressure distributions of fixed and rotating blades; $M_{tip} = 0.44$, $Re = 1.92$ million.

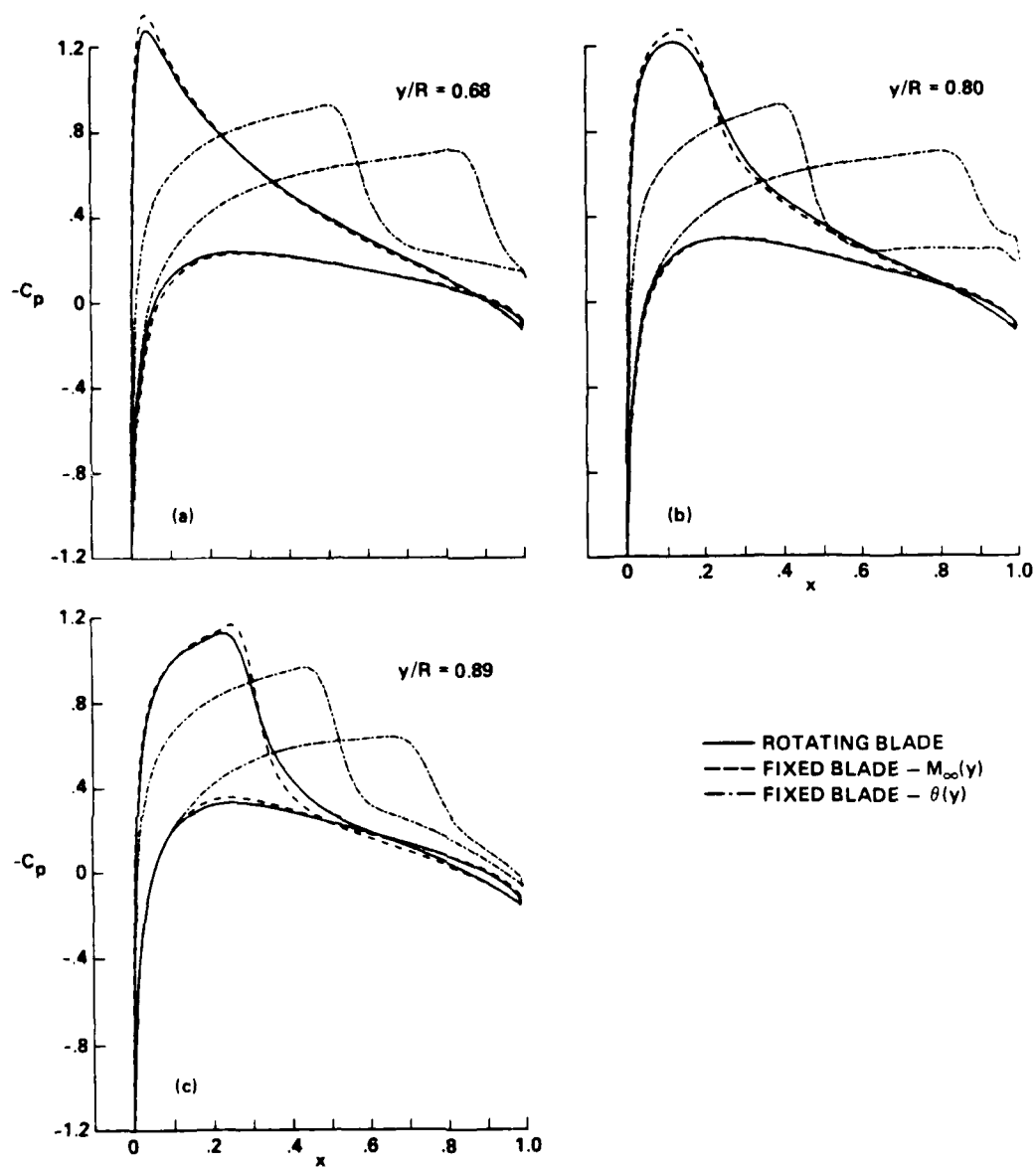


Fig. 12 Comparison of surface pressure distributions of fixed and rotating blades:
 $M_{tip} = 0.877$, $Re = 3.93$ million

END

10-87

DTIC